J. Plasma Phys. (2026), *vol*. 92, E107 © The Author(s), 2026. Published by Cambridge University Press.
This is an Open Access article, distributed under the terms of the Creative Commons Attribution licence (https://creativecommons.org/licenses/by/4.0/), which permits unrestricted re-use, distribution and reproduction, provided the original article is properly cited. doi:10.1017/S0022377826102050

Parallel shock-relevant whistler waves and reflected ions driven by a coaxial plasma gun

Douglass A. Endrizzi[1,2], Joseph Olson[1], Jan Egedal[1], Cary B. Forest[1] and Hiroshi Gota[3]

[1]University of Wisconsin–Madison, Madison, WI, USA
[2]Realta Fusion, Inc., Madison, WI, USA
[3]TAE Technologies, Inc., Foothill Ranch, CA, USA

Corresponding author: Douglass A. Endrizzi, dendrizzi@realtafusion.com

(Received 1 July 2025 UTC; revision received 12 June 2026 UTC; accepted 22 June 2026 UTC)

A flexible laboratory configuration on the Big Red Ball device has been created for studying the physics of parallel shock formation by firing a coaxial plasma gun into a pre-existing plasma along the direction of the background magnetic field. At Alfvén Mach numbers near $M_A \sim 2.4$, we observe this plasma gun piston initiate a dispersive whistler pulse and reflect ions that are collisionless against the background. These reflected ions are focused into an on-axis bunch by a concave-forward potential structure specific to the cylindrical geometry. Resonance of these reflected ions with the dispersive whistler waves, though not observed in the experiment, is a potential mechanism for collisionless shock formation.

Key words: plasma nonlinear phenomena, space plasma physics, plasma dynamics

How do collisionless shocks generate the dissipation necessary to satisfy mass, momentum and energy continuity? For perpendicular shocks, ion reflection and gyration back to the layer are responsible for dissipation beyond resistive or anomalous heating (Forslund *et al.* 1984; Kennel, Edmiston & Hada 2013). In contrast, for quasi-parallel shocks, reflected or shock-heated ions can escape upstream without gyrating back to the layer (Edmiston, Kennel & Eichler 1982). One possible dissipation mechanism posits that these counter-streaming ions steepen foreshock whistler waves until the waves are able to reflect upstream particles, effectively advancing the shock front forward (Burgess 1989; Pantellini *et al.* 1992; Scholer 1993; Chen *et al.* 2021). These steepened pulses merge into a dynamic, non-stationary and extended transition layer, behind which the magnetohydrodynamic continuity equations are ultimately satisfied (Schwartz & Burgess 1991; Scholer, Kucharek & Shinohara 2003; Lucek *et al.* 2008). This inherent non-stationarity of parallel shocks makes *in situ* observations difficult and motivates the development of reproducible laboratory platforms.

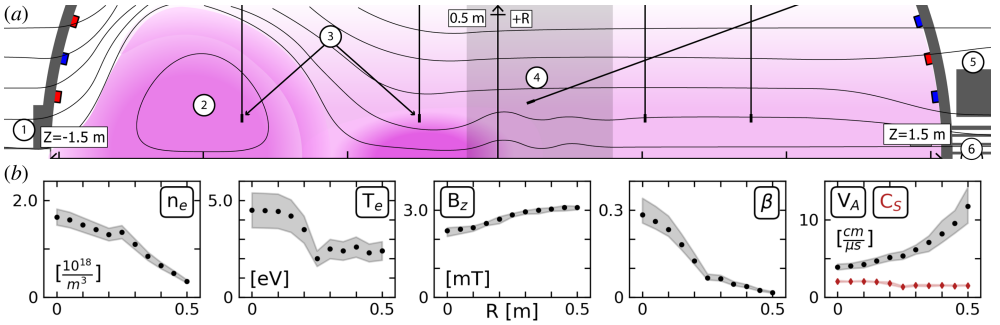


FIGURE 1. (*a*) Cartoon diagram of the experimental set-up during a shot. Guns at the north pole (6) produce the background plasma, which fills the field lines (black) produced with a Helmholtz coil pair (not shown) and a single mirror coil (5). The high-β piston (2) enters the vessel from the coaxial plasma gun barrel (1) and expands radially as it translates. The four hanging double probes (3) are shown at fixed locations of $R = +0.15$ and $Z = -0.86$, -0.25, $+0.52$, $+0.88$ m. The multi-tip Langmuir probe (4) can scan the shaded area. (*b*) The five plots show the initial radial profiles for the primary scan at 3.0 mT field. The coloured-region error bars represent systematic uncertainty, and shot-to-shot fluctuations are smaller.

The substantial challenges to producing properly collisionless parallel shocks in the laboratory means that suitable platforms are scarce. Older pulsed power experiments, which used magnetic pistons with poor shot-to-shot variability, were solidly in the collisional regime (Craig & Paul 1973). Recently, laser platforms have had success in launching collisionless shocks (Fiuza *et al.* 2020), but at parameters where the background magnetic field is dynamically unimportant (i.e. $\beta \equiv P_{\text{plasma}}/P_{\text{mag.}} \gg 1$). Other laser plasma experiments have observed beam instabilities important to quasi-parallel collisionless shocks, but have not observed compression or shock heating (Weidl *et al.* 2017; Heuer *et al.* 2020). The lack of platforms capable of producing large ($L_{\text{exp}} \gg c/\omega_{pi}$), magnetised ($L_{\text{exp}} \gg \rho_i$), collisionless (both $\omega_{ci} \gg \nu_i$ and $\tau_{\text{exp}} < \nu_i^{-1}$) plasmas along with a high-Alfvén-Mach-number ($M_A \equiv u/v_A$) piston means scant experimental work that might corroborate parallel shock models or interpretations of spacecraft observations.

We report a laboratory configuration implemented on the Big Red Ball device at the Wisconsin Plasma Physics Laboratory in which parallel collisionless shock precursors are formed by a nonlinear whistler wave and reflected ions. We are using the word 'precursor' as defined by Schaeffer *et al.* (2020), where we satisfy criteria 1 to 6 but do not see independent reflection of ions from a front that is well separated from the piston. In this experiment, a high-pressure and super-Alfvènic piston collides with a stationary background target plasma. The diamagnetism of the piston plasma sharply bends upstream field lines down to ion-skin-depth scales. This magnetic kink disperses ahead of the piston as whistler waves. A concave-forward potential extends from the piston leading edge that reflects and focuses an ion beam. Measured plasma parameters indicate that the ion beam is fully collisionless. Although the experiment is too short to exhibit cyclic reformation on time scales of several ion cyclotron periods, it demonstrates the ease of producing reflected ions with resonant whistler waves from large-amplitude magnetic perturbations.

To launch the high-pressure piston, a coaxial plasma gun (modelled after one developed for the C-2U experiment (Matsumoto *et al.* 2016)) is mounted on the south pole of the Big Red Ball as shown in figure 1 (Forest *et al.* 2015). The gun is

https://doi.org/10.1017/S0022377826102050 Published online by Cambridge University Press

	n_e (10^{18} m^{-3})	T_e (eV)	B_z (mT)	u_p (cm μs^{-1})	β_e	β_{ram}	f_{ci} (kHz)	$\nu_s^{ii'}$ (kHz)	$\rho_i \equiv c_s/\omega_{ci}$ (m)	d_i (m)	L_i^* (m)
Target	1.6	5	2.6	0	0.3		40		0.13	0.18	
Ion beam	3.5	8	3.5	10	0.9	12	53	5	0.16	0.12	5.3

TABLE 1. Plasma parameters on axis, and estimates of relevant frequencies and lengths. The ion interpenetration length L_i^* is calculated as described by (1).

operated without poloidal bias flux, keeping its internal field low ($|B_{\text{piston}}| \leqslant 0.5$ mT at machine centre), plasma beta high ($\beta_{\text{piston}} \gg 1$) and importantly decreasing the shot-to-shot variability. A 70 μF capacitor bank is charged to 8–10 kV and discharges a primary current I_p of 120–150 kA with a rise time of $\tau_{1/4} \leqslant 5$ μs. The speed of the piston u_p varies from 60 to 150 km s^{-1} and is best controlled by adjusting the delay between the puff valve and main gun triggers, setting the total particle inventory and thus piston mass.

The target hydrogen plasma is produced with an array of washer guns mounted on the north pole, with adjustable total power up to 700 kW and density from $n_e = 0.0$ to 2.0×10^{18} m^{-3} (Fiksel *et al.* 1996). Background neutrals are predominantly hydrogen with a density of $n_n \leqslant 1 \times 10^{17}$ m^{-3}. The axial magnetic field B_z is produced with an external Helmholtz coil pair and can reach 9.0 mT. A weak mirror field around the washer guns (mirror ratio of 3) is used to increase the plasma radius while avoiding a strong axial gradient to the field. Nominal experimental values are listed in table 1 for reference.

With these three experimental knobs of u_p, n_e and B_z, the plasma beta $\beta \equiv 2\mu_0 nT/B^2$ and Alfvén Mach number $M_A \equiv u_p/v_A$ can be controlled. This control is not fully independent, as for non-zero β the plasma diamagnetism weakens the field on axis due to the strong radial gradients (see subplots of figure 1). For low-frequency whistlers ($\omega < \omega_{ce}/2$), such a configuration is well known to duct waves via refraction (Helliwell 1965; Stenzel 1999). This work differs from Stenzel's comprehensive whistler research in a similar cylindrical geometry by our use of a high-beta compact-toroid piston, rather than strong radio-frequency fields, though many of the results are similar. While we explore a wide range of Alfvén ($0 \leqslant M_A \leqslant \infty$) and sonic ($3 \leqslant M \leqslant 6$) Mach numbers, the particular density and magnetic field strength presented in this paper are chosen for their clear whistler signals. For a nominal piston speed of $u_p = 100$ km s^{-1}, the experiment has $M_A \sim 2.4$ on axis but becomes sub-Alfvénic for $R \geqslant 0.45$ m.

The experimental measurements come from four hanging probes at fixed position and a movable probe that can be scanned over a region, as shown in figure 1. The four hanging probes are located at $Z = -0.88, -0.26, +0.52, +0.88$ m and $R = 0.15$ m, with the first and second pairs offset in the azimuthal direction by 60°. Each hanging probe has four planar tips operated as two double probes measuring ion saturation current I_{sat} and an orthogonal set of three $\dot{B}$-coils, all digitised at 10 MHz. These double probes were developed for their resilience to the large plasma potential fluctuations intrinsic to the experiment. However, density measurements from the double probes are calibrated to the colder background plasma and likely overestimate n_e elsewhere. The Langmuir/T_e probe is a 16-tip probe with a three-axis $\dot{B}$-coil set capable of resolving the electron temperature and

https://doi.org/10.1017/S0022377826102050 Published online by Cambridge University Press

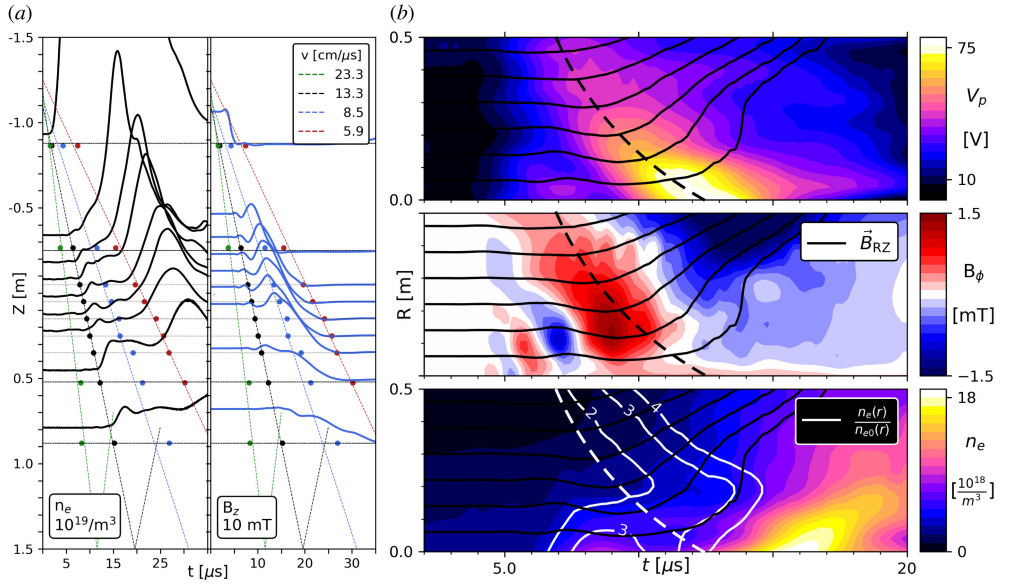


FIGURE 2. (*a*) Measurements of density n_e and axial magnetic field B_z, taken at $R = 0.15$ m and offset in Z. The four colour points (red, blue, black and green) represent locations of peak density (piston centre), magnetic ramp (piston front), earliest density increase (ion beam front) and earliest coherent polarised signals (whistler front), with speeds shown in the upper right. At $t = 12$ μs there is separation of multiple c/ω_{pi} between each. (*b*) Using data from a single radial scan at $Z = -0.1$ m, two-dimensional profiles of plasma potential V_p, toroidal magnetic field B_ϕ and n_e. Black contours are poloidal magnetic field lines. The dashed line follows the V_p peak which forms half of the V-shaped potential. In the centre, the highest frequencies of the whistler pulse arrive at 4 μs. White contours on the bottom plot track where n_e is 2, 3 and 4 times the initial radial value. The ion beam that arrives at 6 μs and $R < 0.2$ m is from focusing of reflected ions towards the axis.

magnetic field up to 5 MHz. That probe scans the shaded region in figure 1, from $Z = -0.1$ to $+0.4$ m and $R = 0.0$ to 0.5 m in 5 cm steps. Radial profiles of the target plasma for this primary scan are shown in figure 1(*b*).

While the target plasma and magnetic field are highly reproducible, the jitter in breakdown of the coaxial plasma gun leads to significant variability in the piston speed. To complete a scan, shots are taken at each T_e probe location until a piston velocity of $u_p = 100 \pm 10$ km s^{-1} is observed, forming a dataset of around 200 shots, with two shots per location. Aligning data between shots requires offsetting in time for shot-to-shot jitter, and, in a few outlier cases, also multiplying the time axis by a factor u_p/u_p^{mean} to correct for the speed.

To show the spatial and temporal development as the piston traverses the vessel, in figure 2(*a*) we plot data from the hanging probes as well as the T_e probe. This plot uses five shots that measured a piston speed of $u_p \sim 85 \pm 5$ km s^{-1}, slower than the 100 km s^{-1} target but with a smaller variance. The T_e probe is at the same radial location $R = 0.15$ m as the hanging probes and is moved in Z between shots. The piston enters from the machine south pole at $Z = -1.5$ m (top of plot) travelling towards the north wall at $Z = 1.5$ m (bottom). We identify the peak piston density in red and the axial field magnetic ramp in blue, which respectively mark the piston centre and leading edge. The earliest rise in density (black) and the earliest coherent

https://doi.org/10.1017/S0022377826102050 Published online by Cambridge University Press

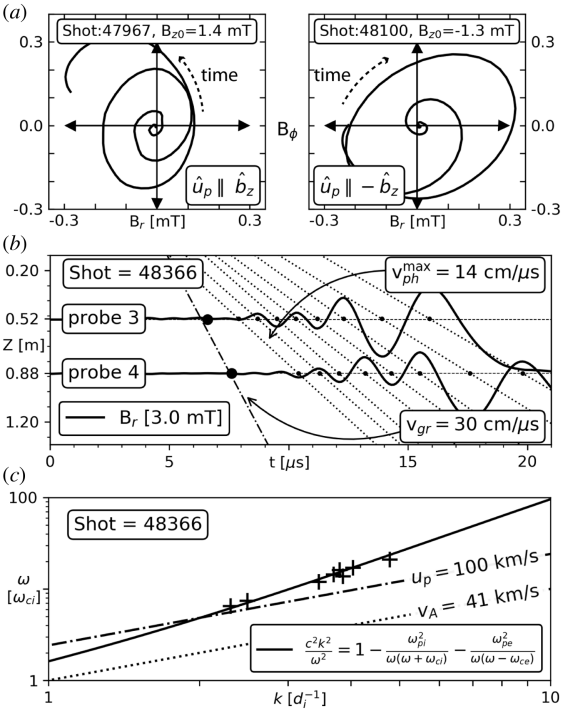


FIGURE 3. (*a*) Hodograms from the $Z = 0.52$ m probe for two shots with the Helmholtz field direction flipped. The wave remains right-hand circularly polarised with respect to the field direction. Peak frequencies are above $20\omega_{ci}$. (*b*) Field B_r traces from the $Z = 0.52$ and 0.88 m probes. The dotted lines estimate the phase velocity $v_{\rm ph}$ while the dash-dotted line estimates the group velocity $v_{\rm gr}$ from the earliest coherent polarised $r\phi$ signal, which is close to the expected $2v_{\rm ph}$. Note also that the highest measured wavenumbers of $\sim$5 are less than the prediction of 2π. (*c*) The R-wave dispersion relation for $B_z = 2.4$ mT and $n_e = 1.6 \times 10^{18}$ m^{-3}. Crosses are values of ω and $k_\parallel$ measured from (*b*), with the Alfvén and piston speeds for reference.

whistler signals (green) are both propagating faster than the piston. When the first whistler signals reach the far wall at $t = 12$ μs, the system has developed for $3\omega_{ci}^{-1}$ and each front is separated by several d_i.

Figure 2(*b*) shows the plasma potential, magnetic field and density from a radial scan of 11 shots from the 100 km s^{-1} dataset. At top, a large V-shaped potential is marked with dashed lines, and a second, smaller potential can be seen on axis 5 μs ahead. In the centre, the toroidal magnetic field B_ϕ is plotted as a colourmap, along with poloidal field lines B_{RZ} plotted in black. At bottom, the high-density piston collides with the target and produces a focused ion beam, visible from 6 to 11 μs and extending out to $R \sim 0.2$ m.

We unambiguously identify these early magnetic waves as whistlers from their right-handed polarisation, the factor of two difference between the peak phase and group velocities and their agreement with the R-wave dispersion relation (figure 3*c*) (Chen 2016). The right-handed polarisation is clearly seen in figure 3(*a*) whereby reversing the background magnetic field flips the rotation direction. In figure 3(*b*), the group velocity of the earliest coherent circularly polarised signals is roughly double the maximum measured phase velocity. The phase velocity measurements,

https://doi.org/10.1017/S0022377826102050 Published online by Cambridge University Press

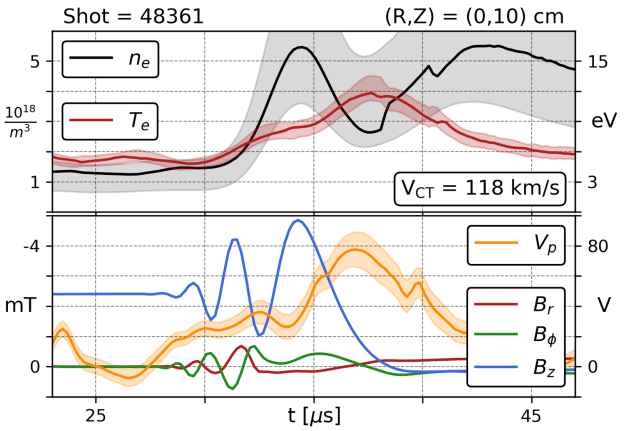


FIGURE 4. The T_e probe time histories of density, temperature, plasma potential and magnetic field. These measurements are taken on the axis, but +20 cm further in Z from the data in figure 2(*b*). The error bars are estimates of the total systematic error including the Langmuir fitting routine, and not the much smaller standard deviation of statistical noise. The potential fluctuations from 23 to 27 μs are global ($\mathrm{d}V_p/\mathrm{d}z = 0$), while the later fluctuations do indicate local electric fields.

taken from the local extrema in the B_r time history, line up within measurement uncertainty along the R-wave dispersion relation in figure 3(*c*). The dot-dash line tracking the group velocity intersects the vessel wall at the same time as the piston enters. From this we infer that the whistler pulse is initiated as the very high-β piston bursts into the vessel and bends the upstream field lines down to an ion-skin-depth-scale length.

This same field-line bending can be seen in the time history of the topmost magnetic trace of figure 2(*a*), which shows the sharpness of this bend 0.6 m away from the entrance at $Z = -1.5$ m. For this near step function in B_z, the B_r component is similar to a delta function of finite width of order c/ω_{pi}. We would expect that a Fourier decomposition then be limited to wavenumbers less than $k = 2\pi/d_i$. If we treat this initial perturbation as a large-amplitude whistler wave that disperses into the upstream (Krasnoselskikh *et al.* 2002), this condition then provides a limit on the production of whistler waves in a piston-driven experiment: if the ramp thickness is limited by the ion skin depth, then waves above $k = 2\pi/d_i$ should not be generated. As expected, figure 3(*c*) shows that the highest measured wavenumbers of $k \sim 5/d_i$ are less than this limit.

More magnetic signals, here taken on axis, can be seen in figure 4 which shows time histories from the T_e probe for a representative shot. The substantial B_z fluctuations are not indicative of oblique propagation but are instead a feature of the wave solution to the cylindrical boundary conditions, akin to an $m = 0$ Helicon mode (Chen 2015). The small B_r and B_ϕ signals are possibly contributions from $m \geqslant 1$ modes from a non-axisymmetric initial piston, a feature that is sometimes seen in fast camera images.

While the experiment's large electron collisionality ($\nu_{e0} \sim 5 \times 10^6\ \mathrm{s}^{-1} \gg \tau_{\mathrm{exp}}^{-1}$) is typical of laboratory plasmas, a high thermal electron collisionality does not preclude collisionless ion behaviour or even acceleration of energetic electrons (Park *et al.* 2015; Fiuza *et al.* 2020). We calculate ion interpenetration lengths L_i^* following

https://doi.org/10.1017/S0022377826102050 Published online by Cambridge University Press

laboratory plasma jet experiment convention (Messer *et al.* 2013; Merritt *et al.* 2014):

$$L_i^* = \frac{u_p}{4\nu_s^{ii'} + \nu_s^{ie'}}, \tag{1}$$

where the ν_s terms are the slowing rates as described in Huba (2013). As shown in table 1, we estimate L_i^* for an upstream particle colliding with the beam to be 5.3 m, which is much larger than the 3 m vacuum vessel. While this suggests that the ions are effectively collisionless, the electrons are everywhere collisional and magnetised ($\omega_{ce} \gg \nu_e \gg \tau_{\exp}^{-1}$). This limits comparison with space plasmas like magnetospheric bowshocks, where electrons are generally collisionless on scales much larger than any shock transition layer.

The concave-forward potential structure reflects ions in an on-axis beam which is visible in figure 2(*b*) from 6 to 11 μs and $R \leqslant 0.2$ m. This moving potential jump is larger than the relative ion kinetic energy $K_i = m_i u_p^2/2 = 52$ eV for $u_p = 100$ km s^{-1} and so can reflect ions. That the beam travels slower than $2u_p$ and that the density increase exceeds two suggest that this is not perfect specular reflection. It is important to understand if this discrepancy is due to dissipation and shock heating, or some other more benign effect.

To investigate this further, we performed a basic Monte Carlo simulation of single-particle ion trajectories in the piston reference frame. We began by recognising that the two-dimensional temporal plots in figure 2(*b*) cannot be simply converted to spatial plots with the Taylor hypothesis because of both the changing velocity and also the dynamic evolution of the structures. Instead, we use the time history of the measured phase velocity from figure 2(*a*) to reconstruct the spatial structure. The resultant static electric and magnetic field structure is used to simulate the trajectories of 10^5 ions with an initial 2 eV thermal distribution impinging at –100 km s^{-1}. The spatial and velocity distributions from this simulation are shown in figure 5. While this model ignores the time evolution of the structure, qualitatively it reproduces the compression in the density by a factor of ∼2.4 and shows a perpendicular ion-beam temperature of $T_\perp \sim 8.6$ eV. These results show that this geometric effect of a concave-forward potential structure can lead to on-axis compression that naively resembles shock compression above the factor of 2 expected for purely reflected ions.

The leading edge of the ion beam satisfies the cyclotron resonance condition with the adjacent whistlers (Gary 1991):

$$\omega - \boldsymbol{k} \cdot \boldsymbol{v}_{\text{beam}} \pm m\omega_{ci} = 0, \tag{2}$$

where m is the harmonic number. Using the wavelength λ at the leading edge of the beam measured from the B_r signals in figure 3, we find for $m = 1$ that $(\omega - m\omega_{ci})/k = 11 \pm 1$ cm μs^{-1}. This is resonant with the beam velocity $v_{\text{beam}} = 13.3$ cm μs^{-1} within a thermal speed ($v_{thi} = 2.0$ cm μs^{-1} at 2 eV). However, the ion beam is well separated from the piston for only 5 μs $\sim \omega_{ci}^{-1}$, which is likely too short for substantial beam–wave coupling (Onsager, Winske & Thomsen 1991). Beam–wave coupling could appear as growth of the amplitude of the plasma potential collocated with the axial magnetic field rarefactions, shown in figure 4 at 30 and 32.5 μs. Given the short duration, we believe we are only seeing the dispersion of the initial steep piston ramp and cannot claim that the whistler waves grow or damp on the ion beam.

Summarising this experiment, we observe the simultaneous production of whistler waves and Doppler-shifted cyclotron resonant reflected ions. To restate the mechanism, a high-pressure supersonic piston creates a steep magnetic ramp and a large

https://doi.org/10.1017/S0022377826102050 Published online by Cambridge University Press

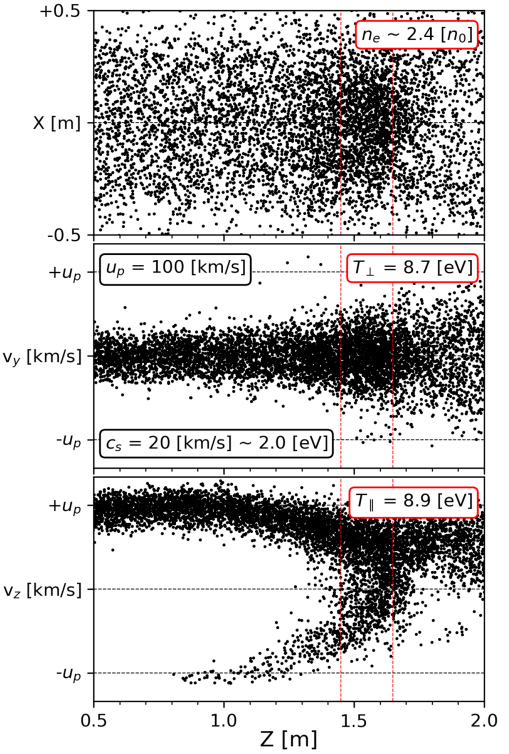


FIGURE 5. Results from a simple Monte Carlo simulation with 10 000 test particles launched towards the static potential derived from the top plot of figure 2(*b*). This simple model roughly reproduces the observed density compression in the reflected ion front.

plasma potential jump. This sharp magnetic feature disperses into super-Alvénic whistler waves. At the same time, the strong plasma potential jump at the piston front specularly reflects ions. These reflected ions are in Doppler-shifted cyclotron resonance with certain whistler wavenumbers and could lead to growth of the whistler wave train, though we do not observe this given the short experiment duration. We reiterate that while the density compression of these reflected ambient ions naively satisfies the Rankine–Hugoniot conditions of a developed shock, this is early in the shock development stage and the ion-reflecting surface has not detached from the piston.

Producing a fully developed shock with the expected Rankine–Hugoniot jump conditions is difficult at these plasma parameters. The prerequisite step of shock detachment, where the potential structure in the leading magnetic field rarefaction grows until it can independently reflect ions, will likely require tens of ion cyclotron periods Onsager *et al.* (1991). Experimentally, this would mean either increasing the magnetic field to extend the effective duration of the experiment such that $L_{\mathrm{exp}}/u_p \gg \omega_{ci}^{-1}$, or repeating this experiment on a larger device. The first option would also require quadratic increases in background density and piston ram pressure to keep β and M_A constant. In either case, maintaining the collisionless ion condition of (1) would be difficult.

An additional experimental challenge is how to inject enough energy into the piston to be effective for the duration of the experiment. As the piston enters the

https://doi.org/10.1017/S0022377826102050 Published online by Cambridge University Press

main vessel and expands, its internal pressure drops adiabatically. This is reflected in the decreasing peak piston density in figure 2(*a*), which is above 10^{20} m^{-3} at the first probe and drops to 10^{19} m^{-3} at the second probe 0.5 m later. When the internal pressure has dropped below the ram pressure $2mv_i^2$ equivalent, the piston is no longer effective. To keep the internal pressure above the ram pressure for the entire duration is a demanding requirement for a pulsed power system on this scale.

Acknowledgements

We would like to acknowledge Department of Energy grant no. DE-SC0018266 for support in the operation of the Wisconsin Plasma Physics Laboratory. These experiments would not have been possible without TAE Technologies, which loaned a magnetised coaxial plasma gun and provided expertise as we developed our own. Thanks also to R. Sassella, J. Wallace and M. Clark for their help in constructing the experiment.

Editor Troy Carter thanks the referees for their advice in evaluating this article.

Declaration of interests

This work was performed while the main author was at the University of Wisconsin-Madison and resubmitted while at Realta Fusion, Inc. The co-authors declare no competing interests.

REFERENCES

BURGESS, D. 1989 Cyclic behavior at quasi-parallel collisionless shocks. *Geophys. Res. Lett.* **16**, 345–348.

CHEN, F.F. 2015 Helicon discharges and sources: a review. *Plasma Sources Sci. Technol.* **24**, 014001.

CHEN, F.F. 2016 *Introduction to Plasma Physics and Controlled Fusion*, 3rd edn. Spring Int'l Publishing.

CHEN, L.-J. *et al.* 2021 Solitary magnetic structures at quasi-parallel collisionless shocks: Formation. *Geophys. Res. Lett.* **48**, e2020GL090800.

CRAIG, A. & PAUL, J. 1973 Observation of a switch-on shock in a magnetized plasma. *J. Plasma Phys.* **9**, 161–186.

EDMISTON, J.P., KENNEL, C.F. & EICHLER, D. 1982 Escape of heated ions upstream of quasi-parallel shocks. *Geophys. Res. Lett.* **9**, 531–534.

FIKSEL, G., ALMAGRI, A., CRAIG, D., IIDA, M., PRAGER, S. & SARFF, J. 1996 High current plasma electron emitter. *Plasma Sources Sci. Technol.* **5**, 78–83.

FIUZA, F. *et al.* 2020 Electron acceleration in laboratory-produced turbulent collisionless shocks. *Nat. Phys.* **16**, 916–920.

FOREST, C. *et al.* 2015 The wisconsin plasma astrophysics laboratory. *J. Plasma Phys.* **81**, 345810501.

FORSLUND, D.W., QUEST, K.B., BRACKBILL, J.U. & LEE, K. 1984 Collisionless dissipation in quasi-perpendicular shocks. *J. Geophys. Res.: Space Phys.* **89**, 2142–2150.

GARY, S.P. 1991 Electromagnetic ion/ion instabilities and their consequences in space plasmas: a review. *Space Sci. Rev.* **56**, 373–415.

HELLIWELL, R.A. 1965 *Whistlers and Related Ionospheric Phenomena*. Stanford University Press.

HEUER, P. *et al.* 2020 Laboratory observations of ultra-low frequency analogue waves driven by the right-hand resonant ion beam instability. *Astrophys. J. Lett.* **891**, L11.

HUBA, J. 2013 *NRL (Naval Research Laboratory) Plasma Formulary*. revised. Naval Research Lab. Report.

KENNEL, C., EDMISTON, J. & HADA, T. 2013 *A Quarter Century of Collisionless Shock Research*, Chap. 1, pp. 1–36. American Geophysical Union (AGU).

KRASNOSELSKIKH, V., LEMBÈGE, B., SAVOINI, P. & LOBZIN, V. 2002 Nonstationarity of strong collisionless quasiperpendicular shocks: theory and full particle numerical simulations. *Phys. Plasmas* **9**, 1192–1209.

https://doi.org/10.1017/S0022377826102050 Published online by Cambridge University Press

LUCEK, E.A., HORBURY, T.S., DANDOURAS, I. & RÈME, H. 2008 Cluster observations of the Earths quasi-parallel bow shock. *J. Geophys. Res.: Space Phys.* **113**, A7.

MATSUMOTO, T. *et al.* 2016 Development of a magnetized coaxial plasma gun for compact toroid injection into the C-2 field-reversed configuration device. *Rev. Sci. Instrum.* **87**, 053512.

MERRITT, E.C., MOSER, A.L., HSU, S.C., ADAMS, C.S., DUNN, J.P., MIGUEL HOLGADO, A. & GILMORE, M.A. 2014 Experimental evidence for collisional shock formation via two obliquely merging supersonic plasma jets. *Phys. Plasmas* **21**, 055703.

MESSER, S., CASE, A., WU, L., BROCKINGTON, S. & WITHERSPOON, F.D. 2013 Nonlinear compressions in merging plasma jets. *Phys. Plasmas* **20**, 032306.

ONSAGER, T.G., WINSKE, D. & THOMSEN, M.F. 1991 Interaction of a finite-length ion beam with a background plasma: reflected ions at the quasi-parallel bow shock. *J. Geophys. Res.: Space Phys.* **96**, 1775–1788.

PANTELLINI, F., HERON, A., ADAM, J. & MANGENEY, A. 1992 The role of the whistler precursor during the cyclic reformation of a quasi-parallel shock. *J. Geophys. Res.* **97**, 1303–1311.

PARK, H.-S. *et al.* 2015 Collisionless shock experiments with lasers and observation of Weibel instabilities. *Phys. Plasmas* **22**, 056311.

SCHAEFFER, D.B., FOX, W., MATTEUCCI, J., LEZHNIN, K.V., BHATTACHARJEE, A. & GERMASCHEWSKI, K. 2020 Kinetic simulations of piston-driven collisionless shock formation in magnetized laboratory plasmas. *Phys. Plasmas* **27**, 042901.

SCHOLER, M. 1993 Upstream waves, shocklets, short large-amplitude magnetic structures and the cyclic behavior of oblique quasi-parallel collisionless shocks. *J. Geophys. Res.: Space Phys.* **98**, 47–57.

SCHOLER, M., KUCHAREK, H. & SHINOHARA, I. 2003 Short large-amplitude magnetic structures and whistler wave precursors in a full-particle quasi-parallel shock simulation. *J. Geophys. Res.* **108**, 1273.

SCHWARTZ, S.J. & BURGESS, D. 1991 Quasi-parallel shocks: a patchwork of three-dimensional structures. *Geophys. Rev. Lett.* **18**, 373–376.

STENZEL, R.L. 1999 Whistler waves in space and laboratory plasmas. *J. Geophys. Res.: Space Phys.* **104**, 14379–14395.

WEIDL, M.S., HEUER, P., SCHAEFFER, D., DORST, R., WINSKE, D., CONSTANTIN, C. & NIEMANN, C. 2017 Towards a parallel collisionless shock in LAPD. *J. Phys.: Conf. Ser.* **900**, 012020.

https://doi.org/10.1017/S0022377826102050 Published online by Cambridge University Press